
Monochromatic Backlighting of Direct-Drive Cryogenic DT Implosions on OMEGA

Introduction

Layered cryogenic DT targets are the baseline approach to achieving ignition in direct-drive inertial confinement fusion (ICF) experiments.^{1,2} Steady progress has been made in experiments with hydrodynamically equivalent,³ energy-scaled implosions^{4–9} on OMEGA.¹⁰

These implosions are designed to achieve similar peak shell velocities (v_{imp}), hot-spot convergence ratios (CR, the ratio of initial ice radius to hot-spot radius), and in-flight aspect ratios (IFAR's) as ignition designs. The IFAR is defined as the ratio of shell radius to shell thickness, given by the full width at $1/e$ density of the shell, when the shell has reached $2/3$ of its initial radius. Recent direct-drive experiments on OMEGA⁹ achieved record performance parameters that when scaled to the laser energy available at the National Ignition Facility (NIF), would achieve a Lawson parameter $P\tau \sim 60\%$ of the value required for ignition,¹¹ where P is the hot-spot pressure and τ is the confinement time. This scaled $P\tau$ is similar to the values achieved in indirect-drive implosions on the NIF.^{12,13}

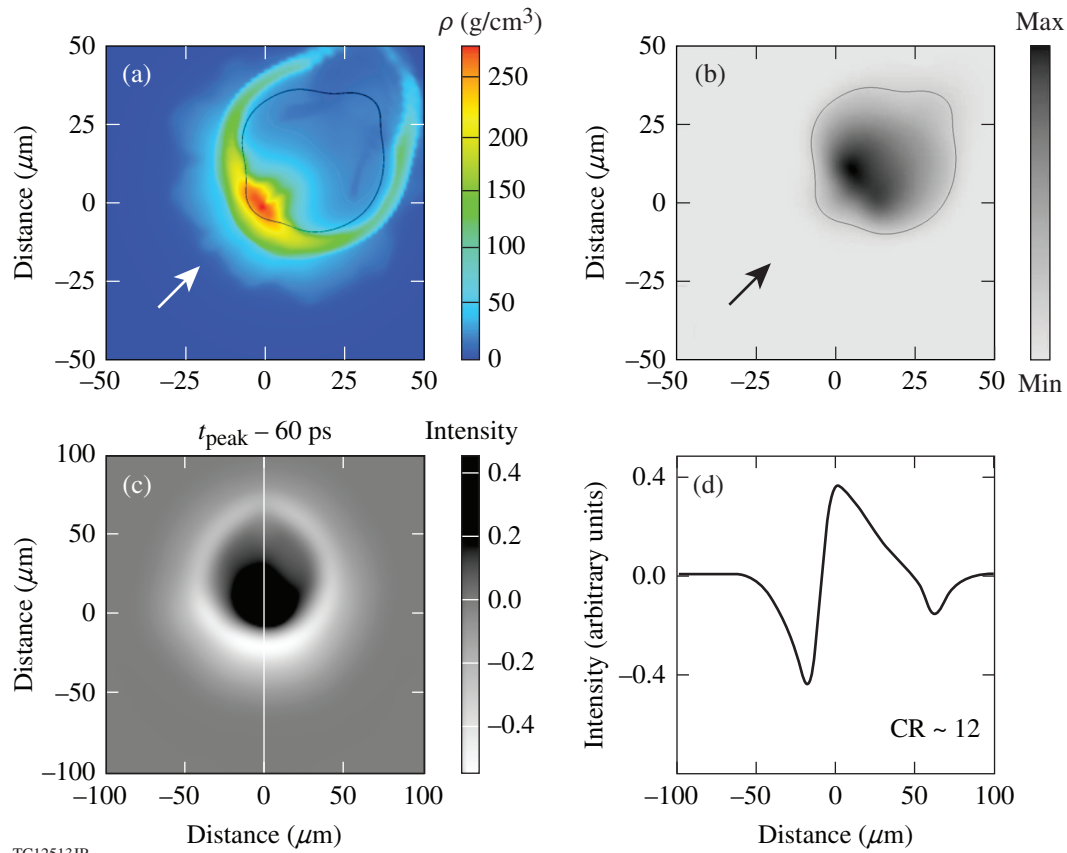
In these experiments the inferred hot-spot pressure P is $\sim 40\%$ lower than one-dimensional (1-D) simulations,⁹ indicating that the experimental performance is significantly degraded. The current hypothesis to explain this performance degradation for implosions with an adiabat ($\alpha > 3.5$ (ratio of shell pressure to the Fermi pressure) is based on low-mode hydrodynamic instabilities.^{8,9,14} These hydro-instabilities can be seeded by long-wavelength nonuniformities in the initial conditions, like ice-thickness variations,⁵ target offset,^{5,15} and laser-drive nonuniformity in space and time (target placement, beam pointing, power balance, and beam timing). Isolated defects like the target stalk,¹⁶ debris on the target surface, or short-wavelength structures like target-surface roughness¹⁷ or laser imprint,^{15,18} especially for low-adiabat implosions ($\alpha < 3.5$), can also seed these instabilities.

The performance of experiments with layered cryogenic DT targets has been measured using nuclear and x-ray self-emission diagnostics.^{8,9} Recent three-dimensional (3-D) hydro

simulations¹⁴ have indicated that the x-ray self-emission images show the influence of long-wavelength nonuniformities on the hot core and do not observe the assembly of the cold shell. Figure 149.31 shows an equatorial density map from 3-D *ASTER* simulations¹⁴ (a) at peak neutron production compared to (b) a simulated self-emission image from an orthogonal polar view in the 4- to 8-keV x-ray band at the same time. The comparison between the density map and a simulated x-ray image demonstrates that the shape of the x-ray image does not follow the density distribution in the shell.

X-ray backlighting can be used to observe the flow of the dense and relatively cold shell material in these cryo DT implosions. This technique has been used successfully in both direct-drive room-temperature experiments with gas-filled plastic (CH) targets¹⁹ and in surrogate indirect-drive²⁰ ICF implosion experiments to measure the velocity and uniformity of the imploding shell. Figure 149.31(c) shows a simulated backlit image 50 ps before peak neutron production at CR ~ 12 . The image is oriented so that the vertical is along the target offset direction. The image shows the absorption of the dense shell as a white ring and the self-emission of the core, which is seen as a darker central feature. The dominant effect from the offset, which will grow into a 5:1 density perturbation at peak compression, is clearly visible in the image and measurable in the lineout [Fig. 149.31(d)], even at this relatively modest convergence.

Direct-drive cryogenic DT implosions on OMEGA are difficult to radiograph because of the low opacity of the DT shell, the high shell velocity, the small size of the stagnating shell, and the very bright self-emission of the hot core. A shaped crystal imaging system with a Si backlighter driven by short (10- to 20-ps) laser pulses from OMEGA EP²¹ was used to radiograph the OMEGA cryogenic implosions. It has the benefits of a narrow spectral width, high photon throughput, and a backlighter with a short emission time and high brightness. Processes with features below the spatial resolution of the imaging system, like mix, can be detected through the opacity effects from the carbon of the ablator material, which will significantly increase



TC12513JR

Figure 149.31

(a) Equatorial distributions of the density from a 3-D radiation–hydrodynamic simulation at peak neutron production taken from Ref. 14. (b) Simulated self-emission image from a polar view in the 4- to 8-keV x-ray band at the same time. The direction of the 20- μm target offset is indicated by an arrow. The thin black line in (b) shows the 17% contour of the maximum x-ray fluence. (c) A simulated backlit image 50 ps before peak neutron production at a convergence ratio (CR) ~ 12 . The image is oriented so that the vertical is along the target offset direction. (d) Vertical lineout through the backlit image.

the absorption of the DT shell if mixing between the ablator and DT shell occurs.

The following sections (1) present the setup of the experiments, including a description of the narrowband crystal imaging system; (2) describe the experimental results in three subsections: (a) low-order modes, (b) stalk effects, and (c) mix; and (3) present our conclusions.

Experimental Setup

The cryogenic targets used in these experiments had an outer radius of ~ 430 to $480 \mu\text{m}$. An ~ 8 - to $12\text{-}\mu\text{m}$ -thick ablator shell of either plastic (CH), deuterated plastic (CD), or CD doped with 0.7% germanium encased a 50- to $75\text{-}\mu\text{m}$ -thick cryogenic DT ice layer [see Fig. 149.32(a)]. All targets were characterized using optical shadowgraphy and showed ice thickness variations of typically $< 1\text{-}\mu\text{m}$ root mean square (rms).⁹ Triple-picket pulses of ~ 22 - to 25-kJ laser energy were used to irradiate the

targets, with smoothing by distributed phase plates (DPP's);²² polarization smoothing (PS) with birefringent wedges;²³ two-dimensional (2-D), three-color-cycle, 0.33-THz smoothing by spectral dispersion (SSD);^{24,25} optimized energy balance ($< 4\%$ beam-to-beam);²⁶ and optimized beam-to-beam timing of ~ 10 -ps rms (Ref. 14). The targets were placed within $\sim 10 \mu\text{m}$ of target chamber center.¹⁴ The shape of the laser pulse was designed to put the shell on a specific adiabat that ranged from ~ 2 to 4 in these experiments. Figure 149.32(b) shows examples of both a lower- and a higher-adiabat pulse at comparable total laser energies. The high-adiabat pulses are shorter and have larger picket energies than the low-adiabat pulses. The total laser energy and the total shell mass determine the peak implosion velocity, which ranged from $v_{\text{imp}} = 2.4$ to 3.7×10^7 cm/s. The IFAR ranged from 10 to 20 in these experiments. The IFAR is predominantly controlled by the shell thickness and shell adiabat.

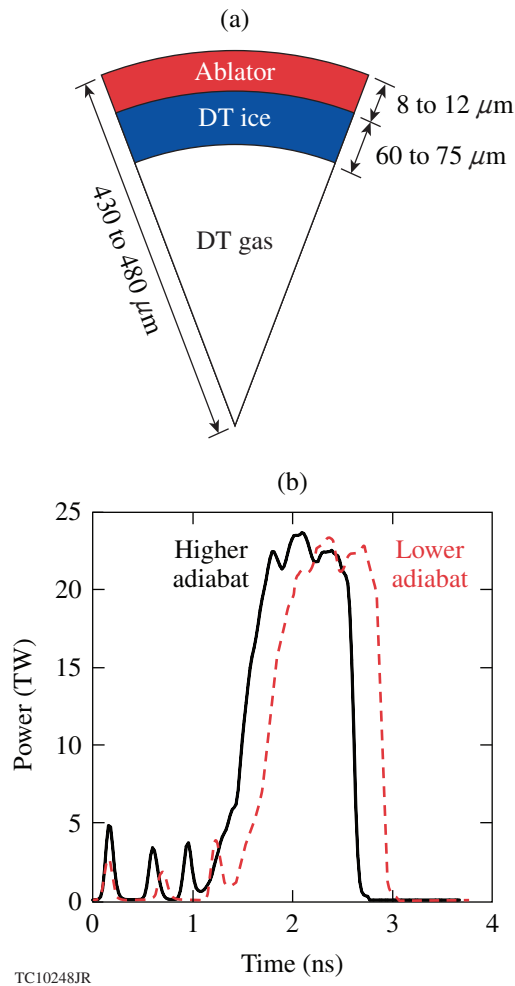


Figure 149.32

(a) The cryogenic DT capsules consist of a thin, 8- to 12- μm -thick CH, CD, or doped-CD ablator filled with several hundred atm of DT gas to create a 60- to 75- μm -thick ice layer at cryogenic temperatures below the triple point of DT ($\sim 19\text{ K}$). (b) The laser drive pulse consists of a series of three pickets to establish the shell adiabat and control shock coalescence and a high-intensity main drive with a total energy of 22 to 25 kJ.

A shaped Bragg crystal-imaging system was used to obtain radiographs of the imploding targets at various convergence ratios. The OMEGA crystal-imaging radiography system²¹ (see Fig. 149.33) uses a Si backlighter driven by the OMEGA EP laser to backlight implosion targets driven by the 60 beams of the OMEGA laser (not shown for clarity). A quartz crystal, cut along the 10 $\bar{1}$ 1 planes for a $2d$ spacing of 0.6687 nm, was used for the Si He $_{\alpha}$ line at $\sim 1.865\text{ keV}$ (0.664 nm). The Bragg angle for this configuration was 83.9° . The crystal was mounted by direct optical contact on an aspheric glass substrate by INRAD.²⁷ The crystal has a major radius of curvature of 500 mm and is placed 267 mm from the implosion target. The

image is recorded on a detector located $\sim 3.65\text{ m}$ from the target, for a magnification of $\sim 15\times$. The quartz crystal is rectangular with a size of $25 \times 10\text{ mm}$, resulting in f numbers of $f = 10$ in the horizontal and $f = 25$ in the vertical direction. The spectral bandwidth of the imager is of the order of 10 eV, which matches the typical broadened linewidth of the resonance line from the backlighter driven by a short-pulse laser.

The available solid angle for the backlighter foil is quite limited since the backlighter target must not intercept any of the 60 beams pointed at the implosion target. Because the backlighter laser intensity must be kept as high as possible, the 500- μm -sq backlighter was placed 5 mm from the implosion target. A fast target insertion system (FASTPOS) inserts the backlighter target 100 ms after the shroud that protects the layered cryogenic target from ambient thermal radiation has been removed. FASTPOS also acts as the direct line-of-sight (LOS) block. Two additional collimators are placed on the mounting structure for the FASTPOS to suppress background from Compton scattering and fluorescence from structures in the target chamber. To reduce the impact of the self-emission of the hot core of the cryo DT implosion, an x-ray framing-camera (XRFC) head²⁸ is used as a detector. The XRFC head is run with either a single-strip microchannel-plate (MCP) detector, with a 300- to 500-ps-long exposure, or a four-strip MCP with an exposure time of $\sim 40\text{ ps}$, where the backlit image is placed in the center of one of the four strips. The spatial resolution of the XRFC recording system is typically $\sim 50\text{ }\mu\text{m}$ (Ref. 29). Experiments with resolution grids show an $\sim 15\text{-}\mu\text{m}$, 10% to 90% edge response for the crystal-imaging system. This spatial resolution is adequate for these initial experiments. Work is underway to improve the resolution to $<10\text{ }\mu\text{m}$. The XRFC is triggered by an ultrastable electro-optical trigger system with

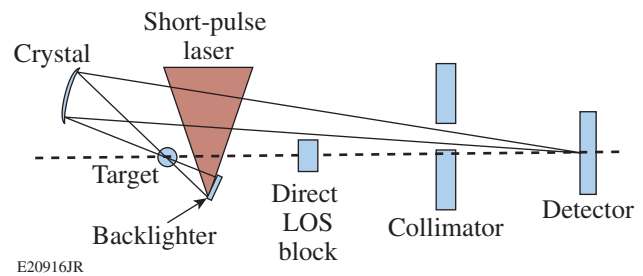


Figure 149.33

Schematic of the spherical-crystal-imager backlighting setup from Ref. 21 (not to scale). The short-pulse laser illuminates a backlighter foil behind the primary target, which is heated by 60 beams from the OMEGA laser (not shown). A direct line-of-sight (LOS) block and a collimator protect the detector [an x-ray framing camera (XRFC)] from background x rays emitted by the backlighter and primary targets.

a jitter of ~ 1.5 -ps rms. Experiments using only the backlighter foil showed that the XRFC system has a jitter of < 10 -ps rms with respect to the arrival of the OMEGA EP laser on the backlighter target. The timing of the OMEGA EP pulse to the OMEGA laser was measured to ~ 10 -ps rms using the neutron temporal diagnostic (P11NTD),³⁰ which is also sensitive to the high-energy x rays produced during the interaction of the OMEGA EP laser with the backlighter target.

Figure 149.34(a) shows the temporal evolution of the implosion from 1-D *LILAC*³¹ simulations close to peak compression compared to the laser pulse shape (blue line) for a typical backlit cryogenic implosion. All *LILAC* simulations shown in this article include the effects of cross-beam energy transfer (CBET)³² and use a nonlocal thermal-conduction model.⁶ The trajectory of the shell radius (peak density: green; $1/e$ of peak density: black) starts at the ~ 430 - μm outer radius of the target and shows the shell moving toward the center until peak compression at ~ 3.5 ns. The neutron-production rate (orange) peaks ~ 40 ps before the calculated areal density (magenta). The exposure time of the XRFC is indicated by the gray-shaded area and the arrival time of the OMEGA EP short-pulse laser by the red vertical line. A time-gated image of a backlit DT cryogenic implosion with an exposure time of ~ 40 ps is shown in Fig. 149.34(b). The dashed white line indicates the original shell diameter, and the white line at the bottom of the image shows the location of the target stalk. The backlighter emission is shown in the center of the image. It is clipped at

the top of the XRFC slit because of a misalignment caused by repeatability issues in the crystal insertion mechanism. The absorption from the compressed shell is seen in the image as a ring-like feature around an emission feature from the central bright core of the implosion.

To measure the absorption in the compressed shell and to quantitatively compare the signal recorded by the crystal imager with simulations, the data must be corrected for the backlighter shape. A simple first-order physical model was constructed²¹ to describe the shape of the backlighter by assuming a constant brightness source. This source was convolved with a Gaussian point-spread function (PSF), representing the spatial resolution of the imaging system at a 5-mm defocus. The brightness and extent of the source and the width of the PSF were varied to obtain a best fit to the shape of the measured signal outside the area affected by the absorption of the target. These uncertainties associated with correction are taken into account in the errors reported on the measured absorption.

Experimental Results

1. Low-Order Modes

Long-wavelength nonuniformity can be seeded in an implosion by a number of processes including nonuniformities in the laser illumination, target placement, and thickness variations in both the ablator and the DT ice layer. To study the impact of these long-wavelength nonuniformities on the assembly of the compressed high-density shell close to stagnation, a series of

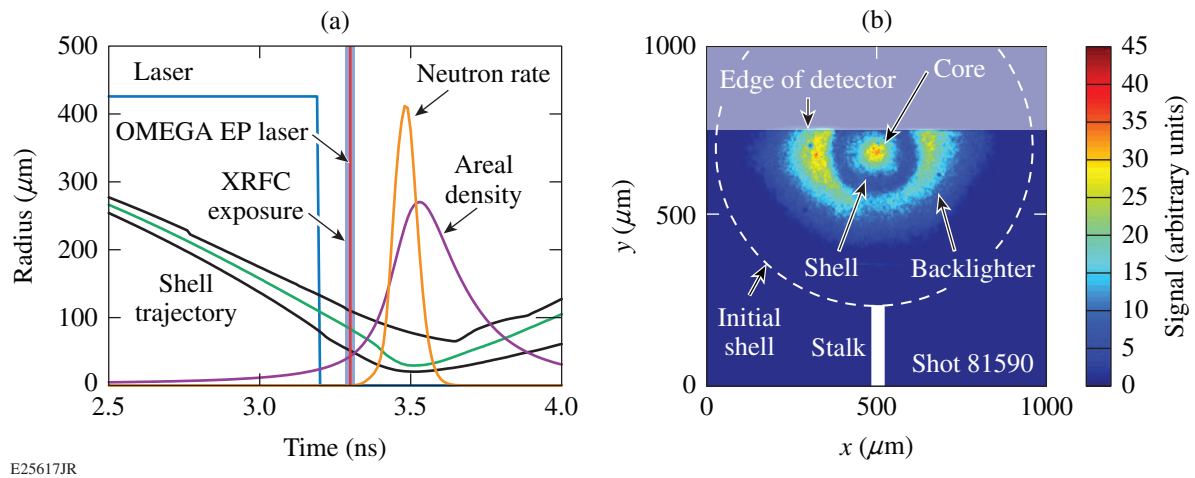
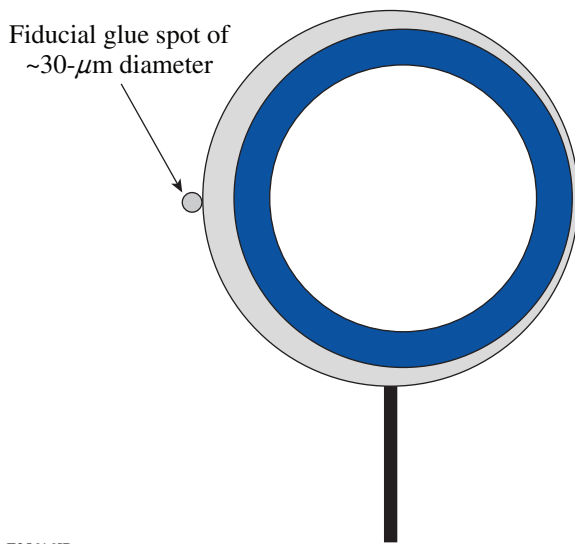


Figure 149.34

(a) Trajectory of the shell radius (center: green; inner, outer edge: black) compared to the temporal history of the laser power (blue) and neutron-production rate (orange) from 1-D *LILAC* simulations for the experiment shown in (b). The areal density evolution is shown for comparison (magenta). The exposure timing of the XRFC is indicated by the vertical gray area and the arrival time of the OMEGA EP short-pulse laser by the red vertical line. (b) Time-gated image of a backlit DT cryogenic implosion with an exposure time of ~ 40 ps. The initial shell radius and the location of the stalk are shown for comparison.

experiments were performed with preimposed initial-thickness perturbations in the CH shell.

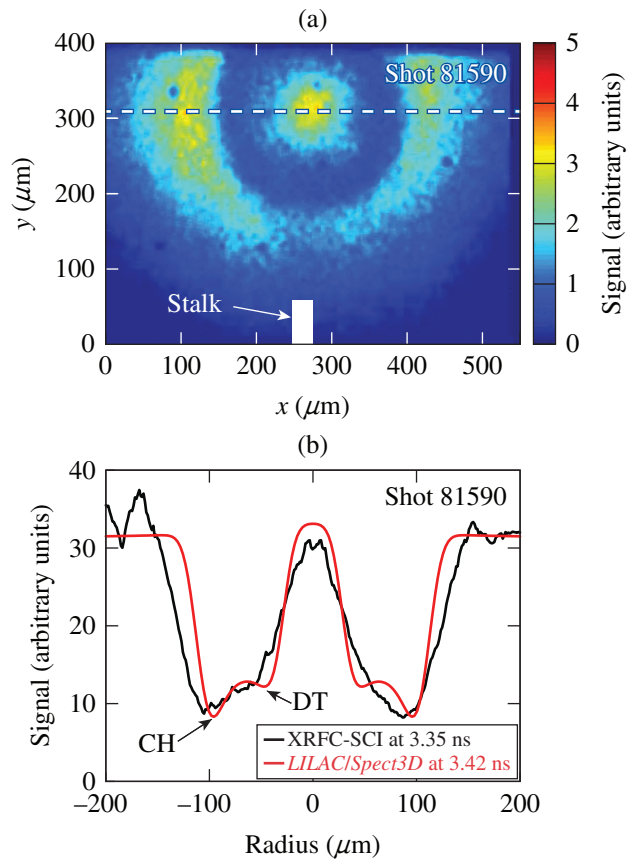
Figure 149.35 illustrates a shaped target with preimposed initial-thickness perturbations in the CH shell. The amplitude of the variation in shell thickness was 2 to 4 μm peak to peak. This variation caused an $\sim 2\text{-}\mu\text{m}$ -rms inner ice radius nonuniformity in the layering process. A fiducial glue spot of $\sim 30\text{-}\mu\text{m}$ diameter was used to orient the target horizontally, i.e., perpendicular to the stalk that is mounted vertically in the target chamber. Standard-quality targets with an ablator-thickness nonuniformity of $<0.1\text{-}\mu\text{m}$ rms in all modes and a DT ice layer nonuniformity of $<1.0\text{-}\mu\text{m}$ rms were used in separate experiments to establish a reference.



E25616JR

Figure 149.35
Illustration of a shaped target with a horizontal variation in CH shell thickness. The amplitude of this variation was 2 to 4 μm peak to peak. This variation caused an $\sim 2\text{-}\mu\text{m}$ -rms nonuniformity in ice thickness. A fiducial glue spot of $\sim 30\text{-}\mu\text{m}$ diameter was used to orient the targets with respect to the stalk.

The radiograph from the reference experiment with a standard-quality target (shot 81590) from Fig. 149.34(b) is shown on an expanded scale in Fig. 149.36(a). The image was recorded at ~ 100 ps before peak neutron production at a CR of 7, with an exposure time of ~ 40 ps. The absorption of the backlighter by the compressed shell is seen in the image as a ringlike feature around a central emission feature from the bright core of the implosion. The initial CH ablator thickness of the target was $\sim 12\ \mu\text{m}$, with an outer diameter of $\sim 890\ \mu\text{m}$. The measured nonuniformity of the outer surface was $0.24\text{-}\mu\text{m}$ rms. The thickness of the DT ice layer was measured at $\sim 61\ \mu\text{m}$ with a $0.5\text{-}\mu\text{m}$ -rms thickness variation. The target was imploded



E25618JR

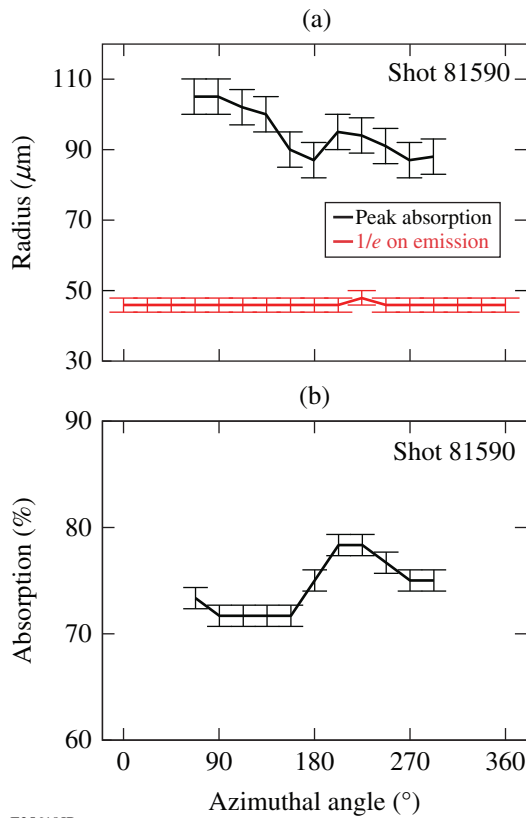
Figure 149.36

(a) Backlit image of cryogenic implosion (shot 81590). (b) Backlighter shape-corrected horizontal lineout compared to *Spect3D* post-processed, 1-D *LILAC* simulations.

with a triple-picket pulse of 24-kJ energy at a calculated adiabat of ~ 2.5 , which led to a calculated IFAR = 10. The measured offset from target chamber center at shot time was $<10\ \mu\text{m}$. The recorded yield was 20% of the 1-D calculations [yield over clean (YOC)] and the measured areal density was $\sim 80\%$ of the predictions.

Figure 149.36(b) shows the backlighter shape-corrected horizontal lineout of the radiograph in Fig. 149.36(a) compared to *Spect3D*³³ post-processed, 1-D *LILAC* simulations. The backlighter intensity was adjusted to match the observed ratio of the backlighter relative to the level of self-emission of the core. The measured spatial resolution of the imager of $\sim 15\ \mu\text{m}$ was taken into account in the *Spect3D* postprocessing. The simulated lineout matches the experiment quite closely in both size and magnitude of the absorption. The most-noticeable difference between experiment and simulation is that the slopes of the signal at the interface between shell and core and at the outside of the shell are significantly steeper in the simulation.

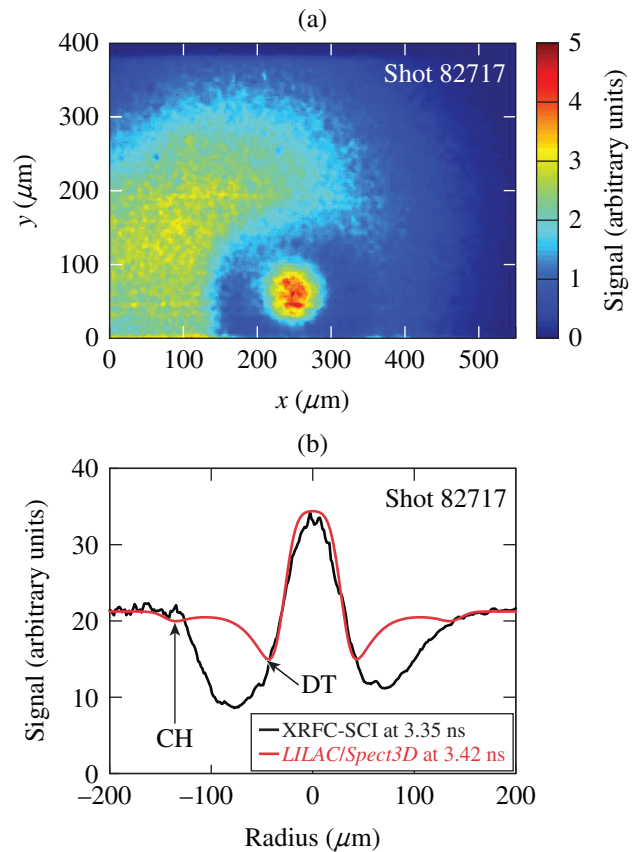
To further analyze the radiographs and to obtain quantitative data on the shape of the compressed shell, radial lineouts were taken from the center of the self-emission peak and the radius of peak absorption and its magnitude were evaluated as a function of azimuthal angle (see Fig. 149.37). The contour at $1/e$ of the peak of the core emission is also determined and plotted in Fig. 149.37(a) for comparison. The errors shown in the graph are estimates of the uncertainty determining the peak absorption location or the $1/e$ of the emission given the signal/noise on the experimental signal. The radius of peak absorption shows predominantly an $\ell = 1$ feature of $\sim 10\text{-}\mu\text{m}$ amplitude, with a small extra feature at 180° azimuthal angle, which is associated with the stalk (see **Stalk Effects**, p. 42). Within the errors of the evaluation, the $1/e$ contour of the core self-emission is observed to be circular. The magnitude of peak absorption shows a small $\sim \pm 5\%$ peak-to-peak variation as a function of angle.



E25619JR

Figure 149.37
 (a) Radius of peak absorption as a function of angle obtained by evaluating lineouts taken from the center of the self-emission peak. The $1/e$ radius contour from the self-emission is shown for comparison. (b) Peak absorption as a function of angle.

A radiograph obtained in an experiment using a shaped target with a $4\text{-}\mu\text{m}$ peak-to-peak variation in the CH ablator wall thickness (shot 82717) is shown in Fig. 149.38(a). The image was recorded at a CR = 10, ~ 50 ps before peak neutron production. The gate time of the XRFC was ~ 40 ps. Because of drifts in the OMEGA EP beam pointing, the registration between the backlighter emission and the implosion is not as good as it was for shot 81590. Nevertheless, the absorption feature from the compressed shell is clearly visible. Since the image was recorded ~ 50 ps closer to peak neutron production and at peak x-ray emission, the emission of the central core is brighter than in the shot shown in Fig. 149.36. The target had an outer diameter of ~ 960 μm with an initial CH ablator thickness of ~ 11 μm . The measured total variation in the radius of the inner DT ice layer was $\sim 2\text{-}\mu\text{m}$ rms and its thickness was ~ 63 μm . The nonuniformity of the outer surface radius was $0.21\text{-}\mu\text{m}$ rms. The target was irradiated with a triple-picket



E25621JR

Figure 149.38
 (a) Backlit image of cryogenic implosion shot 82717 using a shaped target with a $4\text{-}\mu\text{m}$ variation in peak-to-peak CH shell thickness. (b) Backlighter shape-corrected horizontal lineout compared to *Spect3D* post-processed 1-D *LILAC* simulations.

pulse of 25-kJ energy at a calculated adiabat of ~ 2.0 . The calculated IFAR was 14. The measured offset from target chamber center at shot time was $<10 \mu\text{m}$. The observed YOC was 8% and the measured areal density was $\sim 40\%$ of the calculated value.

Figure 149.38(b) shows the backlighter shape-corrected horizontal lineout of the radiograph in Fig. 149.38(a) compared to *Spect3D* post-processed, 1-D *LILAC* simulations, where the backlighter intensity was adjusted to match the observed self-emission of the core. The simulated lineout does not match the experiment quite as well as it did for the comparison shot 81590. While the shape of the self-emission peak is reproduced quite well, the absorption feature from the compressed shell is significantly underestimated. The experimental lineout shows a significant left-right asymmetry, which is consistent with the initial placement of the target, where the thicker side of the CH ablator is placed on the left side of the image shown in Fig. 149.34(a).

The radius of peak absorption and its magnitude are evaluated again as a function of azimuthal angle, together with the contour at $1/e$ of the peak of the core emission (see Fig. 149.39). The radius of peak absorption shows a feature of $\sim 20\text{-}\mu\text{m}$ amplitude. Clipping on the XRFC strip caused by the pointing instability of the crystal-insertion mechanism made it impossible to extract data in the stalk region around the 180° azimuthal angle. The $1/e$ contour of the core self-emission shows a measurable $\ell = 2$ variation with an amplitude of $\sim 7 \mu\text{m}$. A much larger perturbation in the magnitude of peak absorption as a function of an angle of $\sim \pm 20\%$ is observed with the shaped shell compared to the reference shell.

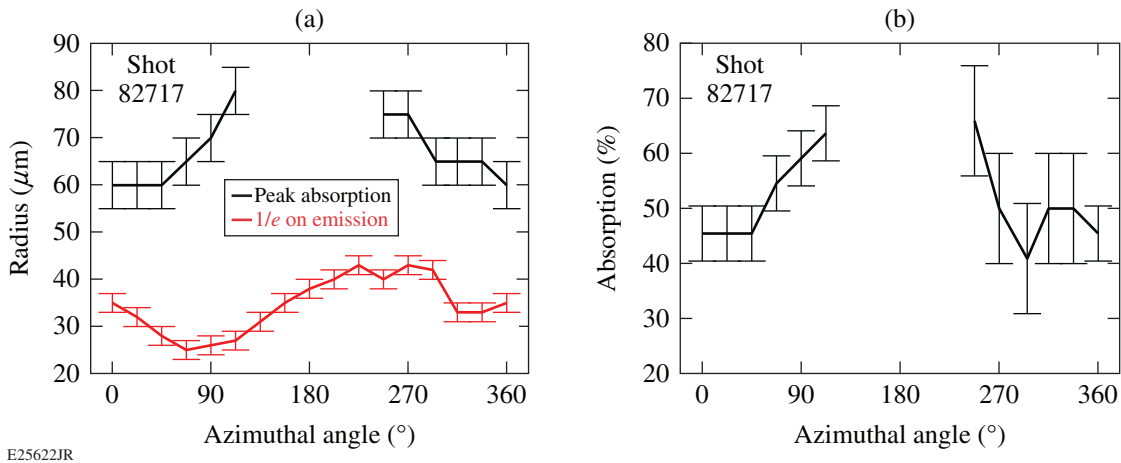


Figure 149.39

(a) Radius of peak absorption as a function of angle obtained by evaluating lineouts taken from the center of the self-emission peak. The $1/e$ radius contour from the self-emission is shown for comparison. (b) Peak absorption as a function of angle.

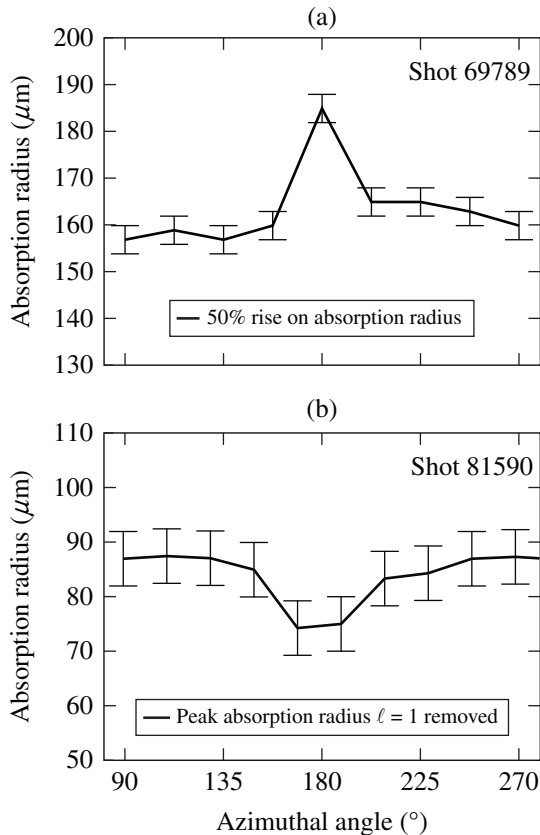
The backlit images show that even for the reference implosion without any preimposed nonuniformity, deviations from a spherical shell assembly can be seen. Additionally, the fact that the interfaces between shell and core and at the outside of the shell are significantly steeper in the simulation indicates that there is probably small-scale mixing occurring in the deceleration phase that cannot be spatially resolved with the imager and therefore is visible only in the change of the gradients compared to the 1-D simulations. The radiograph for the reference implosion also shows that the shape of the dense shell where a significant $\ell = 1$ perturbation is visible, does not necessarily correspond to the shape of the hot spot, which is seen to be round.

The images from the experiments using targets with preimposed CH ablator thickness variations show much larger perturbations than the reference implosion, both in the radius and magnitude of peak absorptions. The lineouts show significantly more absorption over a larger radius than the post-processed 1-D simulation, indicating more mixing between the ablator CH and the DT ice layer. Even though the targets and laser pulses are quite similar, the small differences in both the adiabat and the IFAR lead to significant differences in the shape of the absorption features as compared to simulations.

2. Stalk Effects

The impact of the target stalk and the glue spot, with which the stalk is attached to the shell, on the implosion symmetry has been observed previously using the crystal-imaging system in an implosion experiment with a mass-equivalent CH target fielded from the cryo target insertion system.²¹ At a conver-

gence of 2.5, the image revealed a cusp-like feature in the shell radius at the location of the stalk. Figure 149.40(a) shows the shell radius as a function of azimuthal angle, evaluated at the 50% point on the absorption feature seen in the backlit image of the mass-equivalent CH target (shot 69789). The target had a shell thickness of $24\ \mu\text{m}$ and was irradiated with 23 kJ of laser energy. The evaluation shows a narrow feature of $\sim 25\text{-}\mu\text{m}$ amplitude at the stalk location at 180° azimuthal angle. At the stalk feature, the shell radius is larger than the average shell radius.



E25624JR

Figure 149.40

(a) Shell radius as a function of angle, inferred from the 50% point on the absorption feature seen in the backlit image of a CH target mass equivalent to a cryo target as shown in Ref. 20 (shot 69789). (b) Radius of peak absorption as a function of angle, obtained by taking lineouts from the center of the image from the cryo implosion shown in Fig. 149.35 (shot 81590). An $\ell = 1$ mode of $10\text{-}\mu\text{m}$ amplitude was removed to show the effect of the stalk more clearly.

Figure 149.40(b) shows the radius of peak absorption as a function of angle at a convergence of 7, obtained by taking lineouts from the center of the image from the cryo implosion shown in Fig. 149.35 (shot 81590). An $\ell = 1$ mode of $10\text{-}\mu\text{m}$ amplitude was removed to show the effect of the stalk more

clearly. The radius of peak absorption shows a relatively wide feature of $\sim 45^\circ$ extent in azimuthal angle and an amplitude of $\sim 10\ \mu\text{m}$. In this case the shell radius is smaller at the stalk feature than the average shell radius.

The change in direction of the stalk perturbation from being larger than the average radius at CR = 2.5 during the acceleration phase to being smaller than the average radius at CR = 7 during the deceleration phase is expected based on an analysis of multidimensional hydro simulations. During acceleration, the stalk area lags behind the rest of the shell because the extra mass of the glue and the shadowing of the laser drive by the stalk reduce the shell velocity. During deceleration, the extra mass at the stalk location causes it to decelerate more slowly against the growing pressure of the core, allowing it to push farther in compared to the rest of the shell.

3. Imprint and Mix

The images from most cryogenic DT target experiments show significantly more contrast than expected from *Spect3D* post-processed *LILAC* simulations, which indicates that carbon from the ablator mixes into the DT ice layer.

Figure 149.41 shows a lineout through the image of shot 70535 corrected for the backlighter shape. A 300-ps gate was used in these experiments and was timed to start ~ 500 ps before the calculated time of peak core emission, according to 1-D *LILAC* hydrocode simulations. The OMEGA EP short-pulse laser was fired ~ 100 ps before the end of the gate at a time when the shell assembly was compressed to an inner radius of $\sim 90\ \mu\text{m}$, which translates to a convergence of ~ 4 , given an inner ice shell radius of $\sim 380\ \mu\text{m}$. The calculated areal density of the DT at this convergence was $\sim 14\ \text{mg}/\text{cm}^2$ with an adiabat of 2.5. The simulations show an IFAR = 12 for this implosion.

The result from a 1-D *LILAC* simulation, post-processed with the radiation-transport code *Spect3D*, is plotted for comparison on the left side of the experimental lineout (green line). The backlighter timing had to be shifted ~ 50 ps earlier to match the measured size of the absorption feature, indicating that the implosion was slightly delayed compared to the simulations. The timing of the OMEGA EP laser during these experiments was not as well controlled as it was for the shots with the 40-ps-exposure-time framing camera and had a jitter of the order of 20-ps rms. The measured absorption was much higher than the absorption calculated from the simulations. One possible explanation for this discrepancy is Rayleigh–Taylor mixing of carbon from the outer CD shell into the DT ice during the shell acceleration. Adding a small amount of carbon

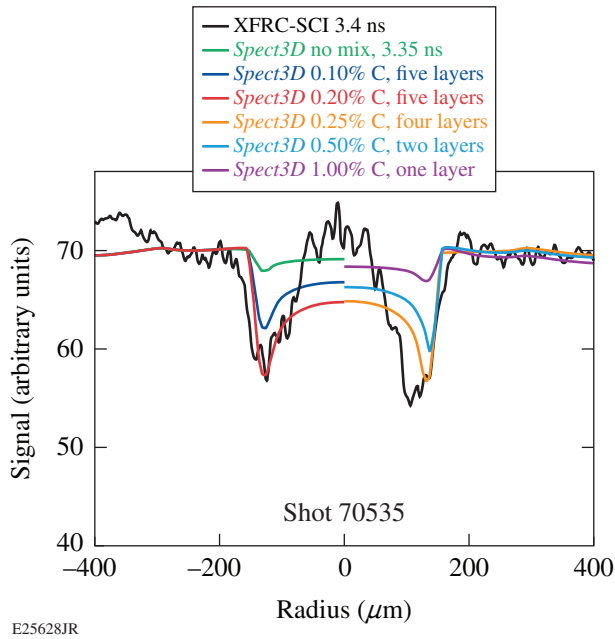


Figure 149.41

Backlighter shape-corrected lineout through the radiograph of a cryogenic target shown in Ref. 21 (black line) compared to *Spect3D* post-processed *LILAC* simulation (colored lines). In the simulation the DT ice was split into five layers and C was uniformly mixed into these layers. The left side of the image shows that simulations with a uniform mix of 0.2% C into the DT match the experimental data (green, blue, and red lines). The right side of the image shows results from simulations where the same mass of C is added to the DT, penetrating into more and more layers (magenta, cyan, orange), showing that at least four layers must be mixed for and adequately matched to the experimental data.

uniformly into the shell in the *Spect3D* postprocessor [0.1% C (blue line), 0.2% C (red line)] significantly increases the absorption in the model and brings the simulation much closer to the experimental data, especially in the areas of highest absorption corresponding to the dense shell. In the center of the image, the calculated absorption with carbon mixing is higher than observed. This is probably caused by a small amount of self-emission, which is not fully suppressed by the gating.

To estimate the depth of the mixing of the carbon into the DT, the DT shell was split into five regions of equal thickness in the 1-D *LILAC* simulations. An equivalent mass of 0.2% C (atomic) was mixed either into the full DT shell or in the outer one, two, or four layers in the *Spect3D* postprocessor. The results from *Spect3D* are shown on the right side of Fig. 149.41. The one-layer simulations (magenta) show almost the same absorption as the unmixed simulations, indicating that the outermost 20% of the DT ice has already ablated at the time the radiograph was recorded, consistent with the predictions from

the 1-D *LILAC* simulations. The two-layer simulation (cyan) shows significantly more absorption but still does not match the experiment. Even the four-layer absorption does not compare as well to the experiment as the fully mixed data, indicating that the carbon is most probably fully mixed throughout the DT shell.

Figure 149.42 shows backlighter shape-corrected lineouts through the radiographs from two additional cryogenic target experiments compared to *Spect3D* post-processed *LILAC* simulations. The lineouts show only one side of the implosion because they could not be corrected for the backlighter shape resulting from a significant misalignment of the backlighter.

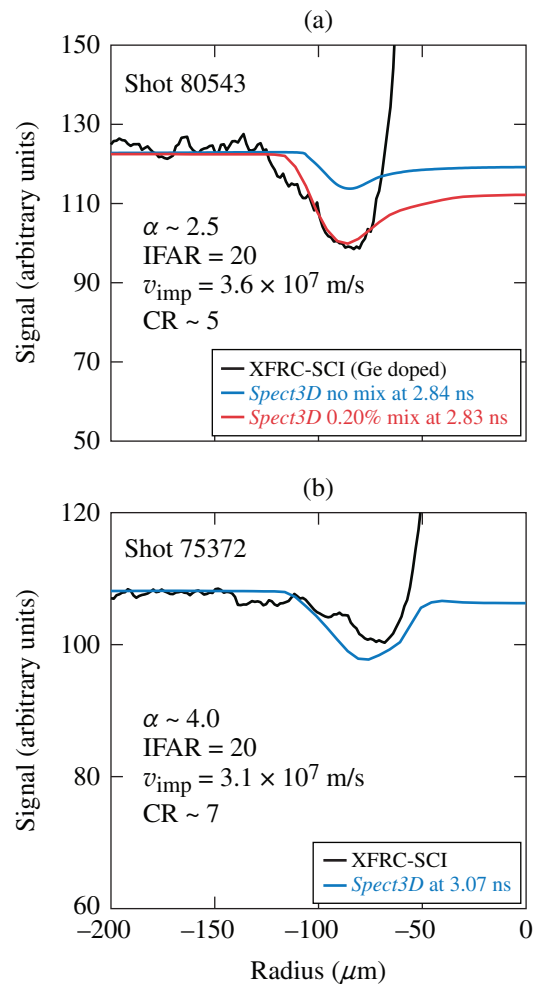


Figure 149.42

Backlighter shape-corrected lineouts through the radiographs from two cryogenic target experiments compared to *Spect3D* post-processed *LILAC* simulations. Mixing of ablator material is required to match the experimental data for a Ge-doped low-adiabat ($\alpha = 2.5$) shot (80543) but not for a high-adiabat ($\alpha = 4.0$) implosion (75372).

The target in shot 80543 had an 8- μm CD shell doped with 0.7% Ge (atomic) and a 50- μm -thick DT ice layer. It was imploded with 25 kJ of laser energy using a pulse that set the calculated adiabat of the shell to 2.5. Preheat from the Ge dopant caused the adiabat to rise to 3.5 at the end of the laser pulse. The IFAR of the shell was calculated to be 20. The radiograph was taken with a 40-ps-wide gate, ~ 150 ps before peak neutron production at a CR = 5 and a predicted areal density of $\sim 40\text{mg}/\text{cm}^2$. Shot 75372 used a target with a 7- μm pure CD shell without any dopant and a 75- μm -thick DT ice layer. It was imploded with 23 kJ of laser energy with a calculated shell adiabat of 4. The calculated IFAR was 20. The radiograph was recorded with a 200-ps XRFC gate, 150 ps before bang time at a CR = 7 and a predicted areal density of $\sim 40\text{mg}/\text{cm}^2$.

Mixing of ablator material at a level of $\sim 0.2\%$ is required to match the experimental data for the low-adiabat, Ge-doped shot (80543), similar to the mix observed in the low-adiabat, pure-CD shot (70535). No indication of mixing is observed in the higher-adiabat implosion (75372). In both radiographs, strong self-emission from the core is observed.

The radiography data show that the most important parameter controlling the mix from the CH/CD outer shell into the ice seems to be the adiabat since even a stable, very low IFAR = 10 implosion (70535) shows significant mix throughout the DT quite early in the implosion at the end of the acceleration phase, well before the onset of deceleration of the shell. Two similar IFAR = 20 implosions show a mix threshold in adiabat at around $\alpha = 4$. The magnitude of the mixing appears to be quite small ($\sim 0.2\%$), which is most likely due to the fact that the DT is starting to be ablated quite early in the implosion. The analysis using five layers for shot 70535 shows that at least the outer 20% of the DT shell gets ablated before the end of the acceleration phase. This ablated DT could serve as a buffer between the CD and the dense DT shell that limits the mix.

Conclusions

X-ray backlighting has been used to radiograph the compressed shell in implosion experiments with layered cryogenic DT targets on OMEGA at convergence ratios from 4 to 10. A shaped-crystal-imaging system with a Si backlighter driven by short laser pulses from OMEGA EP has been set up for this challenging radiography configuration.

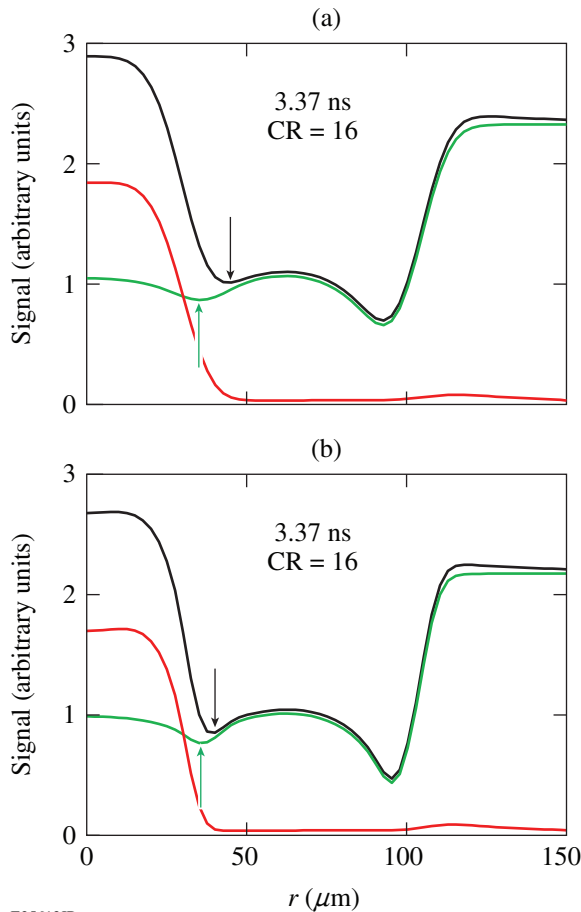
The effects of long-wavelength nonuniformities on the shell assembly close to stagnation have been studied in an experiment with preimposed initial thickness perturbations in the CH shell. The radiograph from the reference implosion without any

preimposed modulations shows a significant $\ell = 1$ perturbation in the shape of the dense shell, which does not match the shape of the hot spot. Additionally, indications of small-scale mixing are observed at the interfaces between ablator, DT shell, and the hot core. The images from targets with preimposed thickness variations show much larger perturbations than the reference implosion, in both the radius and magnitude of peak absorptions and significantly more mixing between the ablator CH and the DT ice layer.

The impact of the target stalk and the glue spot—with which the shell is attached to the stalk—on the implosion symmetry has been observed in both mass-equivalent CH targets and layered DT cryo targets. As expected from simulations, the stalk area lags behind the rest of the shell in the acceleration phase because the extra mass of the glue and the shadow from the stalk reduce the shell velocity and push in farther during the deceleration phase because of the extra mass at the stalk location.

The experimental data show that the most important parameter controlling the mix from the CH/CD outer shell into the ice is the adiabat. A threshold in adiabat at around $\alpha = 4$ has been observed, where mix is below the detection threshold of 0.02%. The magnitude of the mixing appears to be quite small at $\sim 0.2\%$, which is most likely caused by the fact that the DT is starting to be ablated quite early in the implosion, thereby serving as a buffer between the CD and the dense DT shell, which could limit the amount of mix.

Future experiments will use this radiography technique to separate the performance degradation from different sources of nonuniformity, such as target offset and laser energy imbalance, and the experimental data will be compared with detailed multidimensional hydrocode calculations. A project has been started that will improve the spatial resolution of the shaped crystal imager and increase the brightness of the backlighter in order to radiograph the implosions at a higher convergence closer to peak neutron production. To illustrate the benefit from higher spatial resolution, radial lineouts from *Spect3D* post-processed *LILAC* simulations of cryogenic implosions at a convergence ratio of CR = 16 are shown in Fig. 149.43 using either (a) a measured spatial resolution of $\sim 15\ \mu\text{m}$ or (b) an improved resolution of $8\ \mu\text{m}$. The green lines show the absorption of the DT and CH shell, the red lines show the self-emission from the core, and the black lines show the combination of both effects. With the lower resolution of $\sim 15\ \mu\text{m}$, the location of the minimum absorption feature from the DT shell with self-emission, indicated by the black arrows in (a) and (b), is seen at a significantly different radius than the mini-



E25613JR

Figure 149.43

Radial lineouts from *Spect3D* post-processed *LILAC* simulations of cryogenic implosions at a convergence ratio of 16 using (a) a measured spatial resolution of $\sim 15 \mu\text{m}$ and (b) an improved resolution of $8 \mu\text{m}$. The green lines show the absorption of the DT and CH shell, the red lines show the self-emission from the core, and the black lines show the combination of both effects. The black arrows in (a) and (b) indicate the location of the minimum absorption feature from the DT shell with self-emission; the green arrows indicate the minimum absorption without self-emission.

imum absorption without self-emission, indicated by the green arrows. This discrepancy is reduced at the higher resolution of $8 \mu\text{m}$, which will allow one to more-accurately determine the location of the dense DT in the presence of self-emission.

ACKNOWLEDGMENT

This material is based upon work supported by the Department of Energy National Nuclear Security Administration under Award Number DE-NA0001944, the University of Rochester, and the New York State Energy Research and Development Authority. The support of DOE does not constitute an endorsement by DOE of the views expressed in this article.

REFERENCES

1. R. S. Craxton, K. S. Anderson, T. R. Boehly, V. N. Goncharov, D. R. Harding, J. P. Knauer, R. L. McCrory, P. W. McKenty, D. D. Meyerhofer, J. F. Myatt, A. J. Schmitt, J. D. Sethian, R. W. Short, S. Skupsky, W. Theobald, W. L. Kruer, K. Tanaka, R. Betti, T. J. B. Collins, J. A. Delettrez, S. X. Hu, J. A. Marozas, A. V. Maximov, D. T. Michel, P. B. Radha, S. P. Regan, T. C. Sangster, W. Seka, A. A. Solodov, J. M. Soures, C. Stoeckl, and J. D. Zuegel, *Phys. Plasmas* **22**, 110501 (2015).
2. V. N. Goncharov, S. P. Regan, E. M. Campbell, T. C. Sangster, P. B. Radha, J. F. Myatt, D. H. Froula, R. Betti, T. R. Boehly, J. A. Delettrez, D. H. Edgell, R. Epstein, C. J. Forrest, V. Yu. Glebov, D. R. Harding, S. X. Hu, I. V. Igumenshchev, F. J. Marshall, R. L. McCrory, D. T. Michel, W. Seka, A. Shvydky, C. Stoeckl, W. Theobald, and M. Gatu-Johnson, *Plasma Phys. Control. Fusion* **59**, 014008 (2017).
3. V. N. Goncharov, T. C. Sangster, R. Betti, T. R. Boehly, M. J. Bonino, T. J. B. Collins, R. S. Craxton, J. A. Delettrez, D. H. Edgell, R. Epstein, R. K. Follet, C. J. Forrest, D. H. Froula, V. Yu. Glebov, D. R. Harding, R. J. Henchen, S. X. Hu, I. V. Igumenshchev, R. Janezic, J. H. Kelly, T. J. Kessler, T. Z. Kosc, S. J. Loucks, J. A. Marozas, F. J. Marshall, A. V. Maximov, R. L. McCrory, P. W. McKenty, D. D. Meyerhofer, D. T. Michel, J. F. Myatt, R. Nora, P. B. Radha, S. P. Regan, W. Seka, W. T. Shmayda, R. W. Short, A. Shvydky, S. Skupsky, C. Stoeckl, B. Yaakobi, J. A. Frenje, M. Gatu-Johnson, R. D. Petrasso, and D. T. Casey, *Phys. Plasmas* **21**, 056315 (2014).
4. C. Stoeckl, C. Chiritescu, J. A. Delettrez, R. Epstein, V. Yu. Glebov, D. R. Harding, R. L. Keck, S. J. Loucks, L. D. Lund, R. L. McCrory, P. W. McKenty, F. J. Marshall, D. D. Meyerhofer, S. F. B. Morse, S. P. Regan, P. B. Radha, S. Roberts, T. C. Sangster, W. Seka, S. Skupsky, V. A. Smalyuk, C. Sorce, J. M. Soures, R. P. J. Town, J. A. Frenje, C. K. Li, R. D. Petrasso, F. H. Séguin, K. Fletcher, S. Padalino, C. Freeman, N. Izumi, R. Lerche, and T. W. Phillips, *Phys. Plasmas* **9**, 2195 (2002).
5. F. J. Marshall, R. S. Craxton, J. A. Delettrez, D. H. Edgell, L. M. Elasky, R. Epstein, V. Yu. Glebov, V. N. Goncharov, D. R. Harding, R. Janezic, R. L. Keck, J. D. Kilkenny, J. P. Knauer, S. J. Loucks, L. D. Lund, R. L. McCrory, P. W. McKenty, D. D. Meyerhofer, P. B. Radha, S. P. Regan, T. C. Sangster, W. Seka, V. A. Smalyuk, J. M. Soures, C. Stoeckl, S. Skupsky, J. A. Frenje, C. K. Li, R. D. Petrasso, and F. H. Séguin, *Phys. Plasmas* **12**, 056302 (2005).
6. V. N. Goncharov, T. C. Sangster, P. B. Radha, R. Betti, T. R. Boehly, T. J. B. Collins, R. S. Craxton, J. A. Delettrez, R. Epstein, V. Yu. Glebov, S. X. Hu, I. V. Igumenshchev, J. P. Knauer, S. J. Loucks, J. A. Marozas, F. J. Marshall, R. L. McCrory, P. W. McKenty, D. D. Meyerhofer, S. P. Regan, W. Seka, S. Skupsky, V. A. Smalyuk, J. M. Soures, C. Stoeckl, D. Shvarts, J. A. Frenje, R. D. Petrasso, C. K. Li, F. Séguin, W. Manheimer, and D. G. Colombant, *Phys. Plasmas* **15**, 056310 (2008).
7. T. C. Sangster, V. N. Goncharov, R. Betti, T. R. Boehly, D. T. Casey, T. J. B. Collins, R. S. Craxton, J. A. Delettrez, D. H. Edgell, R. Epstein, K. A. Fletcher, J. A. Frenje, V. Yu. Glebov, D. R. Harding, S. X. Hu, I. V. Igumenshchev, J. P. Knauer, S. J. Loucks, C. K. Li, J. A. Marozas, F. J. Marshall, R. L. McCrory, P. W. McKenty, D. D. Meyerhofer, P. M. Nilson, S. P. Padalino, R. D. Petrasso, P. B. Radha, S. P. Regan, F. H. Seguin, W. Seka, R. W. Short, D. Shvarts, S. Skupsky, V. A. Smalyuk, J. M. Soures, C. Stoeckl, W. Theobald, and B. Yaakobi, *Phys. Plasmas* **17**, 056312 (2010).

8. T. C. Sangster, V. N. Goncharov, R. Betti, P. B. Radha, T. R. Boehly, D. T. Casey, T. J. B. Collins, R. S. Craxton, J. A. Delettrez, D. H. Edgell, R. Epstein, C. J. Forrest, J. A. Frenje, D. H. Froula, M. Gatu-Johnson, V. Yu. Glebov, D. R. Harding, M. Hohenberger, S. X. Hu, I. V. Igumenshchev, R. Janezic, J. H. Kelly, T. J. Kessler, C. Kingsley, T. Z. Kosc, J. P. Knauer, S. J. Loucks, J. A. Marozas, F. J. Marshall, A. V. Maximov, R. L. McCrory, P. W. McKenty, D. D. Meyerhofer, D. T. Michel, J. F. Myatt, R. D. Petrasso, S. P. Regan, W. Seka, W. T. Shmayda, R. W. Short, A. Shvydky, S. Skupsky, J. M. Soures, C. Stoeckl, W. Theobald, V. Versteeg, B. Yaakobi, and J. D. Zuegel, *Phys. Plasmas* **20**, 056317 (2013).
9. S. P. Regan, V. N. Goncharov, I. V. Igumenshchev, T. C. Sangster, R. Betti, A. Bose, T. R. Boehly, M. J. Bonino, E. M. Campbell, D. Cao, T. J. B. Collins, R. S. Craxton, A. K. Davis, J. A. Delettrez, D. H. Edgell, R. Epstein, C. J. Forrest, J. A. Frenje, D. H. Froula, M. Gatu Johnson, V. Yu. Glebov, D. R. Harding, M. Hohenberger, S. X. Hu, D. Jacobs-Perkins, R. T. Janezic, M. Karasik, R. L. Keck, J. H. Kelly, T. J. Kessler, J. P. Knauer, T. Z. Kosc, S. J. Loucks, J. A. Marozas, F. J. Marshall, R. L. McCrory, P. W. McKenty, D. D. Meyerhofer, D. T. Michel, J. F. Myatt, S. P. Obenshain, R. D. Petrasso, R. B. Radha, B. Rice, M. Rosenberg, A. J. Schmitt, M. J. Schmitt, W. Seka, W. T. Shmayda, M. J. Shoup III, A. Shvydky, S. Skupsky, S. Solodov, C. Stoeckl, W. Theobald, J. Ulrich, M. D. Wittman, K. M. Woo, B. Yaakobi, and J. D. Zuegel, *Phys. Rev. Lett.* **117**, 025001 (2016); **117**, 059903(E) (2016).
10. T. R. Boehly, D. L. Brown, R. S. Craxton, R. L. Keck, J. P. Knauer, J. H. Kelly, T. J. Kessler, S. A. Kumpan, S. J. Loucks, S. A. Letzring, F. J. Marshall, R. L. McCrory, S. F. B. Morse, W. Seka, J. M. Soures, and C. P. Verdon, *Opt. Commun.* **133**, 495 (1997).
11. A. Bose, K. M. Woo, R. Betti, E. M. Campbell, D. Mangino, A. R. Christopherson, R. L. McCrory, R. Nora, S. P. Regan, V. N. Goncharov, T. C. Sangster, C. J. Forrest, J. Frenje, M. Gatu Johnson, V. Yu. Glebov, J. P. Knauer, F. J. Marshall, C. Stoeckl, and W. Theobald, *Phys. Rev. E* **94**, 011201(R) (2016).
12. O. A. Hurricane *et al.*, *Nature* **506**, 343 (2014).
13. R. Betti, A. R. Christopherson, B. K. Spears, R. Nora, A. Bose, J. Howard, K. M. Woo, M. J. Edwards, and J. Sanz, *Phys. Rev. Lett.* **114**, 255003 (2015).
14. I. V. Igumenshchev, V. N. Goncharov, F. J. Marshall, J. P. Knauer, E. M. Campbell, C. J. Forrest, D. H. Froula, V. Yu. Glebov, R. L. McCrory, S. P. Regan, T. C. Sangster, S. Skupsky, and C. Stoeckl, *Phys. Plasmas* **23**, 052702 (2016).
15. S. X. Hu, V. N. Goncharov, P. B. Radha, J. A. Marozas, S. Skupsky, T. R. Boehly, T. C. Sangster, D. D. Meyerhofer, and R. L. McCrory, *Phys. Plasmas* **17**, 102706 (2010).
16. I. V. Igumenshchev, F. J. Marshall, J. A. Marozas, V. A. Smalyuk, R. Epstein, V. N. Goncharov, T. J. B. Collins, T. C. Sangster, and S. Skupsky, *Phys. Plasmas* **16**, 082701 (2009).
17. I. V. Igumenshchev, V. N. Goncharov, W. T. Shmayda, D. R. Harding, T. C. Sangster, and D. D. Meyerhofer, *Phys. Plasmas* **20**, 082703 (2013).
18. S. X. Hu, D. T. Michel, A. K. Davis, R. Betti, P. B. Radha, E. M. Campbell, D. H. Froula, and C. Stoeckl, *Phys. Plasmas* **23**, 102701 (2016).
19. P. B. Radha, F. J. Marshall, J. A. Marozas, A. Shvydky, I. Gabsalski, T. R. Boehly, T. J. B. Collins, R. S. Craxton, D. H. Edgell, R. Epstein, J. A. Frenje, D. H. Froula, V. N. Goncharov, M. Hohenberger, R. L. McCrory, P. W. McKenty, D. D. Meyerhofer, R. D. Petrasso, T. C. Sangster, and S. Skupsky, *Phys. Plasmas* **20**, 056306 (2013).
20. D. G. Hicks, B. K. Spears, D. G. Braun, R. E. Olson, C. M. Sorce, P. M. Celliers, G. W. Collins, and O. L. Landen, *Phys. Plasmas* **17**, 102703 (2010).
21. C. Stoeckl, M. Bedzyk, G. Brent, R. Epstein, G. Fiksel, D. Guy, V. N. Goncharov, S. X. Hu, S. Ingraham, D. W. Jacobs-Perkins, R. K. Jungquist, F. J. Marshall, C. Mileham, P. M. Nilson, T. C. Sangster, M. J. Shoup III, and W. Theobald, *Rev. Sci. Instrum.* **85**, 11E501 (2014).
22. Y. Lin, T. J. Kessler, and G. N. Lawrence, *Opt. Lett.* **20**, 764 (1995).
23. T. R. Boehly, V. A. Smalyuk, D. D. Meyerhofer, J. P. Knauer, D. K. Bradley, R. S. Craxton, M. J. Guardalben, S. Skupsky, and T. J. Kessler, *J. Appl. Phys.* **85**, 3444 (1999).
24. S. Skupsky, R. W. Short, T. Kessler, R. S. Craxton, S. Letzring, and J. W. Soures, *J. Appl. Phys.* **66**, 3456 (1989).
25. S. P. Regan, J. A. Marozas, R. S. Craxton, J. H. Kelly, W. R. Donaldson, P. A. Jaanimagi, D. Jacobs-Perkins, R. L. Keck, T. J. Kessler, D. D. Meyerhofer, T. C. Sangster, W. Seka, V. A. Smalyuk, S. Skupsky, and J. D. Zuegel, *J. Opt. Soc. Am. B* **22**, 998 (2005).
26. F. J. Marshall, J. A. Delettrez, R. Epstein, R. Forties, R. L. Keck, J. H. Kelly, P. W. McKenty, S. P. Regan, and L. J. Waxer, *Phys. Plasmas* **11**, 251 (2004).
27. Inrad Optics, Northvale, NJ 07647.
28. D. K. Bradley, P. M. Bell, O. L. Landen, J. D. Kilkenny, and J. Oertel, *Rev. Sci. Instrum.* **66**, 716 (1995).
29. J. A. Oertel, T. Archuleta, C. G. Peterson, and F. J. Marshall, *Rev. Sci. Instrum.* **68**, 789 (1997).
30. C. Stoeckl, R. Boni, F. Ehrne, C. J. Forrest, V. Yu. Glebov, J. Katz, D. J. Lonobile, J. Magoon, S. P. Regan, M. J. Shoup III, A. Sorce, C. Sorce, T. C. Sangster, and D. Weiner, *Rev. Sci. Instrum.* **87**, 053501 (2016).
31. J. Delettrez, R. Epstein, M. C. Richardson, P. A. Jaanimagi, and B. L. Henke, *Phys. Rev. A* **36**, 3926 (1987).
32. I. V. Igumenshchev, D. H. Edgell, V. N. Goncharov, J. A. Delettrez, A. V. Maximov, J. F. Myatt, W. Seka, A. Shvydky, S. Skupsky, and C. Stoeckl, *Phys. Plasmas* **17**, 122708 (2010).
33. Prism Computational Sciences, Inc., Madison, WI 53711.